ARTICLE

doi:10.1038/nature15512

Single cell activity reveals direct electron transfer in methanotrophic consortia

Shawn E. McGlynn[1]†*, Grayson L. Chadwick[1]*, Christopher P. Kempes[2,3,4] & Victoria J. Orphan[1]

Multicellular assemblages of microorganisms are ubiquitous in nature, and the proximity afforded by aggregation is thought to permit intercellular metabolic coupling that can accommodate otherwise unfavourable reactions. Consortia of methane-oxidizing archaea and sulphate-reducing bacteria are a well-known environmental example of microbial co-aggregation; however, the coupling mechanisms between these paired organisms is not well understood, despite the attention given them because of the global significance of anaerobic methane oxidation. Here we examined the influence of interspecies spatial positioning as it relates to biosynthetic activity within structurally diverse uncultured methane-oxidizing consortia by measuring stable isotope incorporation for individual archaeal and bacterial cells to constrain their potential metabolic interactions. In contrast to conventional models of syntrophy based on the passage of molecular intermediates, cellular activities were found to be independent of both species intermixing and distance between syntrophic partners within consortia. A generalized model of electric conductivity between co-associated archaea and bacteria best fit the empirical data. Combined with the detection of large multi-haem cytochromes in the genomes of methanotrophic archaea and the demonstration of redox-dependent staining of the matrix between cells in consortia, these results provide evidence for syntrophic coupling through direct electron transfer.

Ecological processes are fundamentally spatial in nature: those governing microbial organisms are no exception. The ubiquity and impact of biofilms, consortia, and other multicellular assemblages in the fields of environmental microbiology, industry, and medicine demonstrates the necessity of relating the spatial position of cells to metabolic activity and community function[1–7]. Theoretical modelling[8] and laboratory experiments with artificial co-cultures[4,9] have offered fundamental insights regarding the effect of spatial architecture on the fitness and physiology of interacting populations, but studying the influence of spatial organization on uncultured microorganisms has remained a long-standing challenge. To translate information learned from modelling and derived laboratory results to systems found in nature requires new methodological strategies that are capable of elucidating microbial structure–activity relationships.

Here, fluorescence *in situ* hybridization and nanoscale secondary ion mass spectrometry (FISH–nanoSIMS) combined with ^{15}N stable isotope probing was used to investigate how single-cell metabolic activity is related to cellular configuration in highly structured, bi-species microbial consortia in environmental samples (Fig. 1 and Extended Data Fig. 1). We applied these methods to empirically test long-standing hypotheses regarding the metabolic interactions underpinning the environmentally important microbial symbiosis responsible for the anaerobic oxidation of methane (AOM) in ocean sediments[10–13]. Discovered over a decade ago[10], these consortia consist of multiple lineages of as yet uncultured anaerobic methanotrophic archaea (ANME) and sulfate-reducing Deltaproteobacteria (SRB), and form diverse aggregate configurations within methane seep sediments worldwide[14,15]. Initial FISH–SIMS acquired whole aggregate stable isotope depth profiles offered isotopic evidence for the involvement of ANME–SRB consortia in anaerobic methanotrophy[11] and documented broad anabolic activity patterns amongst different AOM aggregate morphologies[16], but key questions regarding the mechanism of this syntrophic association remain. There are a number of hypotheses regarding the metabolic interactions underlying this enigmatic methane-fueled symbiosis, ranging from classical syntrophy based on hydrogen, formate or acetate[17,18], to less conventional forms of metabolite or reducing equivalent exchange (for example, methanethiol and disulfide)[19,20]. Understanding whether there is a universal mechanism controlling ANME–SRB mediated methane oxidation or if different archaeal–bacterial AOM consortia use a variety of syntrophic strategies, is still an unresolved question in the field.

Independent of the specific mechanism, a key prediction regarding syntrophic associations of microbes is that the spatial arrangement of paired organisms can greatly influence the metabolic activity of individual cells[12,13,21,22]. In these cases, homogeneous species mixing is expected to facilitate efficient transfer of diffusible intermediates and lead to enhanced metabolic activity[13,22]. Similarly, at the single-cell level, syntrophic partners in immediate proximity to one another are expected to gain a greater metabolic benefit in comparison to cells that lack a syntrophic interface. For the AOM system, these predictions are captured in previously published models[12,13] and also in examples presented here (Extended Data Fig. 2) which are based on syntrophic transfer[23] or commensal passage[20] of a diffusible intermediate. Notably, these modelling results are at odds with the frequent documentation of large environmental consortia with spatially segregated ANME and SRB cells and it remains unclear how these configurationally segregated consortia persist, and often dominate, if they are at a disadvantage to those that are well mixed[10,16]. The discrepancies between *in situ* observations and model predictions motivate a series of hypotheses that are testable with single-cell biosynthetic activity measurements of AOM consortia: (1) within highly segregated consortia, the vast majority of activity will be restricted to cells at interfaces between syntrophic partners, and (2) that segregated syntrophic consortia will have lower total activity levels on average

[1]Division of Geological and Planetary Sciences, California Institute of Technology, Pasadena, California 91125, USA. [2]Exobiology Branch, National Aeronautics and Space Administration Ames Research Center, Moffett Field, California 94035, USA. [3]Control and Dynamical Systems, California Institute of Technology, Pasadena, California 91125, USA. [4]SETI Institute, Mountain View, California 94034, USA.
†Present address: Department of Biological Sciences, Tokyo Metropolitan University, Tokyo 192-0397, Japan.
*These authors contributed equally to this work.

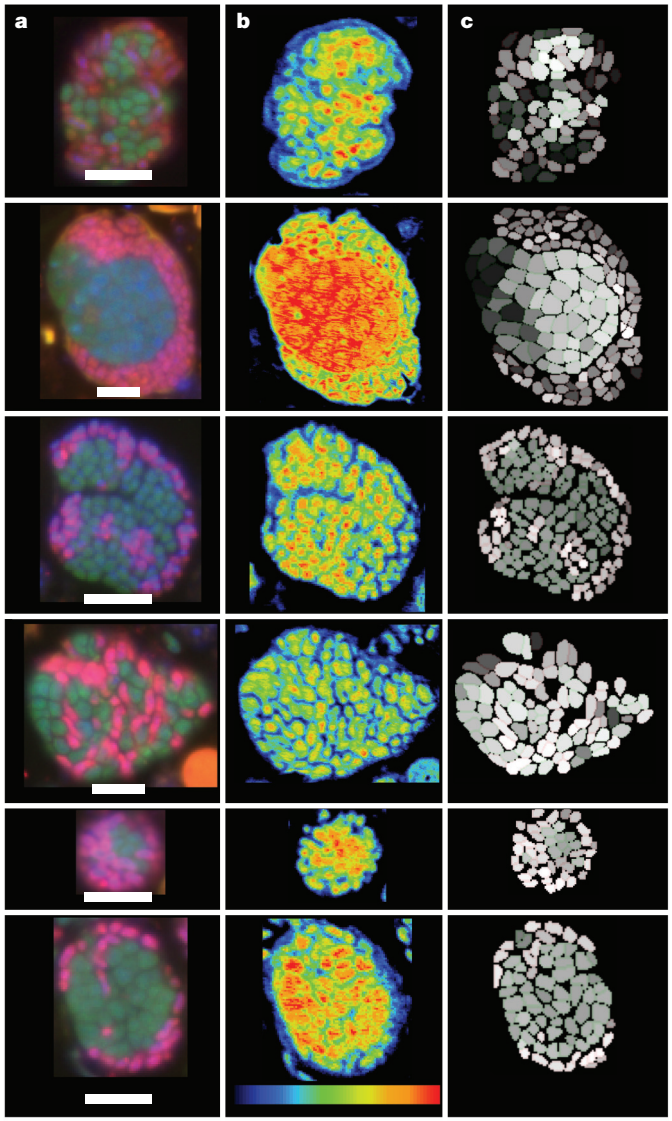

Figure 1 | Examples of AOM consortia identified by FISH and paired anabolic activity measurement via nanoSIMS. **a**, FISH-identified consortia showing archaeal cells (green) and Deltaproteobacteria (pink). The top two panels represent consortia of ANME-2c or 2b paired with Deltaproteobacteria. The lower four panels show ANME-2c archaea paired with the seep-specific deltaproteobacterial group, SEEP-SRB1a. Scale bars, 3 μm. **b**, Corresponding nanoSIMS ion images of biomass show $^{14}N^{12}C^-$ ion images with warmer colours indicating higher secondary ion counts (maximum 1,500 counts). **c**, Single cell activities are measured as ^{15}N atom percentages for regions of interest (ROI) representing the FISH-identified archaea and bacteria in each consortium. Lighter shaded cells are more enriched in ^{15}N, which corresponds with higher levels of anabolic activity and $^{15}NH_4^+$ assimilation. Representative aggregates were chosen from the larger data set composed of 62 aggregates.

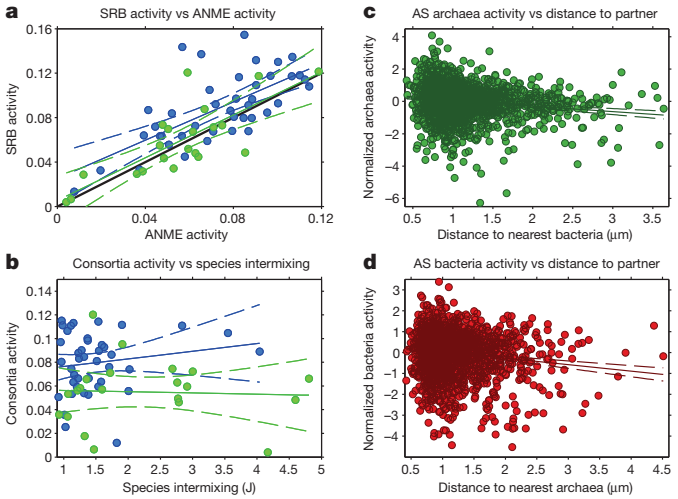

Figure 2 | Activity relationships between archaea and bacteria in AOM consortia. **a**, Population-level average of bacterial activity versus archaeal activity for individual AOM consortia revealing a positive correlation in activity between paired partners. Individual AS aggregates shown in blue ($n = 41$, $R^2 = 0.47$), AD in green ($n = 21$, $R^2 = 0.62$). The 1:1 line is shown in black. **b**, Total consortium activity plotted against the join index (J) of spatial intermixing between archaeal and bacterial partners, where lower J values represent greater mixing (AS in blue: $n = 41$, $R^2 = 0.03$; AD in green: $n = 21$, $R^2 = 0.00$). **c**, **d**, Activity of single archaeal or bacterial cells, respectively, plotted against distance to the nearest syntrophic partner for the AS data set (**c**, $n = 1{,}967$, $R^2 = 0.02$; **d**, $n = 2{,}067$, $R^2 = 0.02$). The equivalent analysis for AD is provided in Extended Data Fig. 6. In all plots R^2 values and solid lines represent linear regressions of the plotted data. Dashed lines illustrate the 95% confidence intervals in slopes and intercepts of the linear regressions.

relative to well-mixed consortia. If these patterns of activity are not observed, then the interactions driving the symbiosis may be distinct from the classical view of syntrophy occurring through the exchange of a diffusible chemical intermediate.

These hypotheses were evaluated for phylogenetically diverse ANME-2 archaea (belonging to the order Methanosarcinales) and partner Deltaproteobacteria using high-resolution biosynthetic activity measurements paired with FISH-based microbial identification; giving us the ability to catalogue cell activity, phylogeny, and cellular position within consortia. ^{15}N-ammonium assimilation, used as a marker for biosynthetic activity[16,24], was determined for 5,453 FISH-identified cells within 62 consortia from a deep-sea sediment incubation showing AOM activity, allowing an assessment of the biosynthetic activity of each cell as it relates to spatial positioning of adjacent syntrophic partners (Fig. 1). Two different groups of co-occurring AOM consortia in the incubation were analysed: 41 archaeal aggregates paired with the specific Desulfobacteraceae lineage SEEP-SRB1a which have been observed as a common bacterial partner of ANME-2 worldwide[25] (AS; ANME-2c: SEEP-SRB1a), and 21 archaeal aggregates paired with other, non-SEEP-SRB1a Deltaproteobacteria (AD; ANME-2c or ANME-2b: Deltaproteobacteria); (Fig. 1, Extended Data Fig. 3 and Supplementary Information).

Spatial patterns of cellular activity

FISH analyses of AS and AD aggregates revealed nearly equal abundances of archaea and bacterial cells within each consortia (Extended Data Fig. 3). The average activity (^{15}N enrichment) of archaeal and bacterial populations from each consortia was found to be correlated and close to the 1:1 line suggesting a beneficial metabolic interaction (Fig. 2a), although the AS bacteria were on average slightly more active than their archaeal partners (Extended Data Fig. 4). The AS and AD consortia analysed in this study occupied a considerable range of both biosynthetic activity and cell number (Extended Data Fig. 3). In order to relate this range of activity to the amount of partner intermixing, we developed a quantitative metric, J, to describe aggregate spatial mixing (Extended Data Fig. 5 and Supplementary Discussion). J values for aggregates represented a range of mixing, and permutation tests revealed that the majority of AS and AD consortia exist in conformations where partnering cells were more segregated than could be explained by random chance, consistent with patterns emerging from binary cell division (Extended Data Fig. 5). Across this conformational variability however, the degree of mixing between cell types (J values between 0.9 and 4.8) did not influence the average biosynthetic activity of the entire consortium (Fig. 2b), indicating the overall activity of well-mixed consortia (low J values) was not greater than those that were segregated.

When examining the ^{15}N-based activity patterns of individual archaeal and bacterial cells within a consortium, each cell's activity

was found to be unrelated to proximity to the nearest archaeal or bacterial partner (Fig. 2c, d and Extended Data Fig. 6). Similarly, in the vast majority of consortia, the cells located at syntrophic interfaces were not significantly more active than those surrounded by the same cell type (Supplementary Tables 1–4, and Extended Data Fig. 7). These single cell measurements are consistent with previously published results of intact AOM consortia, where a correlation between bulk ^{15}N enrichment and natural abundance $\delta^{13}C$ (a proxy for methanotrophic ANME biomass) in SIMS depth profiles was not detected[16]. We also examined whether archaeal or bacterial cellular activity was related to the external environment, however no significant correlation with distance to the aggregate–environment interface was observed (Extended Data Fig. 8). These observations are contrary to conventional diffusive model results for syntrophic AOM partners[12,13] in scenarios where one or both partners are dependent on the surrounding environment (Extended Data Fig. 2 shows diffusion model results for a broad range of diffusion and activity rates). Other potential relationships between total consortia activity and aggregate size approximated from total cell number, as well as the relative ratio of ANME and SRB cells in each consortium were also not significant in our data set (R^2 values <0.04).

Diffusion versus direct electron transfer

The distance-independent trends in cellular activity presented in Fig. 2b–d, Extended Data Fig. 6, and Supplementary Tables 1–4 are in stark contrast to what is predicted in the case of syntrophic exchange[12,13] or commensal sharing[20] of a diffusible intermediate (see diffusion model results in Extended Data Fig. 2 and Supplementary Information). To explore diffusion-independent scenarios which might explain our empirical data, we constructed a second generalized model that captures the basic features of direct interspecies electron transfer[26]. This model is based on electron export by one cell type and electron import by a partner within the consortia, where electrons are able to freely flow across the entire aggregate with a dependence on electric potential (Supplementary Information). Consistent with our data, these models predict a reduction in the overall correlation between biosynthetic activity and aggregate geometry (J metric), especially as the electric conductivity of the aggregate is increased relative to the growth rates (Extended Data Fig. 9). In particular, total aggregate activity is relatively insensitive to how well mixed the aggregate is, and single-cell activities are less correlated with the distance to either the aggregate surface or the syntrophic partner (Extended Data Fig. 9). In both models (Extended Data Figs 2 and 9), the empirical results presented in Fig. 2 are best matched with an increased ratio of metabolic exchange rates relative to cellular activity rates and both models converge to similar results for high rates of transport. For a diffusible intermediate, this ratio would need to be larger than predictions from known intermediate diffusivities[13], our observed growth rates, and the expected growth yields.

These model results related to the J metric illustrate key geometric and mechanistic differences beyond those stemming from spatial gradients. We find that in the low transport regimes for both the diffusive and electric conductivity models, the total activity of consortia is strongly related to the overall mixing between the two partners, but with opposite and somewhat unanticipated outcomes. As predicted, the slow relative transport diffusion scenario shows the highest activity associated with well-mixed consortia (low J values), however, the electron conductivity model indicates higher levels of activity in more segregated consortia (high J values); (Extended Data Fig. 9a). This prediction arises because our conductive treatment of the consortia relies on the global electric potential for each consortia, which is strongest when the electron producing and consuming cells are spatially segregated, maximizing polar charge separation. It should also be noted that mechanisms of electron diffusion[27,28] would produce relative transport rates sufficient for matching the observed equable activity patterns (Supplementary Discussion).

Multi-haem cytochrome genes in ANME-2 genomes

Motivated by these modelling results in which direct electron transfer apparently relaxes spatial controls on aggregate activity in agreement with our single cell observations, we analysed available ANME-2 genomes to determine whether there were signs of this alternative mode of syntrophy as has been previously suggested for ANME-1 (ref. 29). Remarkably, the genomes of two recently sequenced methanotrophic archaea (ANME-2a[30] and ANME-2d[31]), as well as a reconstructed metagenomic bin corresponding to the ANME-2b (data not shown) were each found to encode large multi-haem cytochromes (MHCs), including the largest described from an archaeon to date (34 haems); (Fig. 3a, b). A subset of these previously overlooked MHCs occur fused with a single putative S-layer domain which appears to be a homologue of the S-layer protein in *Methanosarcina acetivorans* (Fig. 3a), suggesting MHC export from the cell and incorporation into the archaeal S-layer. The occurrence of MHCs of this size encoded in a genome is rare even in bacteria, and those that do occur are almost exclusively found in organisms known to conduct extracellular electron transfer such as *Geobacter* and *Shewanella* — species which serve as model organisms for the process[26,32–34].

Cytochrome reactive staining in consortia

To test possibility that MHCs are positioned between cells within consortia as electron conduits, the cytochrome reactive histochemical stain 3,3′-diaminobenzidine (DAB)[35] was applied to AOM consortia recovered directly from sediment. Treatment with DAB and H_2O_2 followed by post fixation with OsO_4 resulted in the staining of: (1) the cellular membranes of both syntrophic partners, (2) some intra-cellular membrane invaginations of paired Deltaproteobacteria, and (3) the extracellular space between cells within consortia (Fig. 3c, d). DAB staining with the addition of H_2O_2 was observed in many, but not all aggregates in the preparation, suggesting the possibility of phylogenetic or phenotypic variation in extracellular MHC production within the sediment-hosted AOM consortia. No visible staining was observed in control experiments without H_2O_2 (Fig. 3e, f). As DAB is known to react with redox active transition metal ions (including those bound by haem groups within cytochromes) in the presence of H_2O_2[36], these results are consistent with the localization of the respiratory chain in the cellular membrane for each organism, and also with the presence of haem proteins capable of redox activity in the space between cells in consortia.

A model for direct electron transfer

The electron microscopy results reported above, together with the presence of the large MHCs in all available ANME-2 genomes suggests that extracellular electron transfer may be an important feature of the anaerobic methanotroph lifestyle. Based on this finding, and the lack of genomic evidence presented for other syntrophic models[20], we propose the catabolic model for AOM coupled to extracellular electron transfer depicted in Fig. 4. Using known biochemical coupling mechanisms in methanogens[37], the oxidation of one mole of methane can result in four moles of reduced methanophenazine. We propose that these methanophenazines are oxidized by an integral membrane protein (for example, cytochrome *b*), with electrons being transferred onto an initial MHC for transport from the membrane to the S-layer. Tandem proteins 2566125773 and 2566125774 in the ANME-2a genome encode a predicted formate dehydrogenase-related cytochrome *b* and an 11-haem multi-haem cytochrome, which are possible candidates for this methanophenazine:cytochrome *c* oxidoreductase step. The MHC/S-layer fusion proteins depicted in Fig. 3a could then be used for electron transport across the S-layer. Finally, large extracellular cytochromes such as the 31 CxxCH motif containing protein 2566123495 and numerous other small MHC proteins could be used to confer electrical conductivity to the exopolymer matrix between the ANME-2 archaea and their SRB partners, similar to the case of MHC proteins thought to facilitate growth of thick geobacter biofilms[26]. As formulated here, this proposed metabolic pathway could potentially

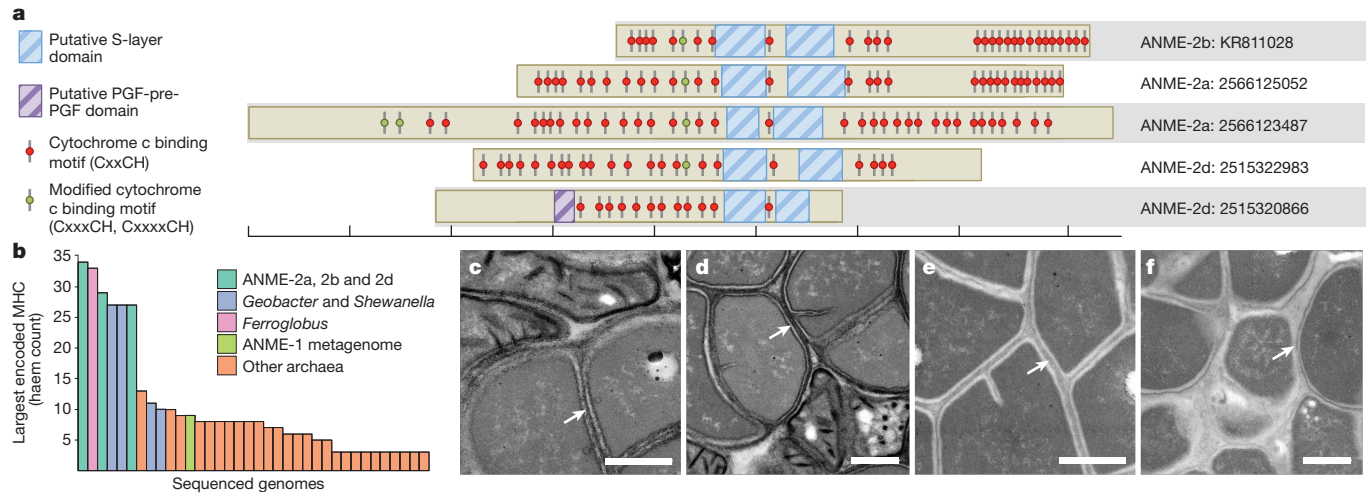

Figure 3 | Multi-haem cytochrome genes, genomes and TEM visualization of haem group reactivity in representative ANME–SRB consortia. **a**, Five MHCs with predicted S-layer domains from reconstructed ANME-2 genomes. Cytochrome *c* binding motif sites (CxxCH) are indicated by red dots, alternative binding motifs (CxxxCH and CxxxxCH) are shown in green. Putative S-layer domains and potential PGF-pre-PGF archaeosortase recognition domains as predicted by the NCBI conserved domain database are shown in blue and purple, respectively. Protein schematics are simply positioned to show compositional similarity, not sequence alignment. Each vertical tick-mark denotes 250 amino acids. The gene identifier numbers are shown on the right. **b**, Size of largest MHC present in sequenced archaeal genomes with representative model bacteria, *Geobacter* and *Shewanella*, included as a reference. **c**–**f**, Transmission electron microscopy (TEM) micrographs of sediment-hosted methanotrophic consortia treated with the haem-reactive compound 3′-3-diaminobenzadine (DAB). **c**, **d**, Positive staining of the membranes and extracellular space between archaeal and bacterial cells in the presence of H_2O_2. **e**, **f**, Control cells from DAB experiments where H_2O_2 was omitted. Scale bars, 500 nm. Arrows mark the interfaces of cells.

result in the net translocation of ~$2H^+$ per CH_4 oxidized by the ANME-2 archaea, with some uncertainty due to the exact stoichiometry of the proton and sodium pumping complexes involved. This low proton efflux per substrate used fits well with the small thermodynamic free energies associated with anaerobic oxidation of methane[23] and the slow growth rates of these organisms.

Together, the evidence from our spatially resolved analysis of cellular activity, genomic observations, and electron microscopy experiments is highly suggestive of direct interspecies electron transfer between methanotrophic ANME-2 and associated Deltaproteobacteria. This diffusion-independent mechanism appears to largely obviate the geometric constraints amongst ANME–SRB consortia. Interspecies electron transfer may also contribute to greater stability of the association compared with syntrophic exchange of a diffusible intermediate, where loss to the environment and greater sensitivity to environmental chemical fluctuations can limit otherwise favourable thermodynamics. The type of interspecies electronic coupling described here and in co-cultured organisms for example[38,39], (and see also ref. 26 and references therein), may be an underappreciated natural phenomenon that contributes to microbial niche construction, where metabolic coupling facilitated by direct electron transfer could function as a means of generating stable syntrophic microbial assemblages. Additionally, the MHCs in ANME-2 genomes may help explain the occurrence of ANME-2 aggregates without syntrophic partners, as well as the observation of AOM with metal oxides, where the ANME-2 may be able to grow on their own as metal oxide reducers[40]. Future work will be required to fully comprehend the detailed mechanisms of electron transfer, the role of MHCs, and the potential function of interspecies electron transfer among different ANME groups or habitats. The culture-independent approach described here is applicable to investigating interactions occurring in a broad range of environmental microbial assemblages and may be amenable with other stable isotope tracers (for example, deuterated water), where the central challenge is to understand how metabolic interconnectivity and spatial relationships between organisms drives local and bulk geochemical processes.

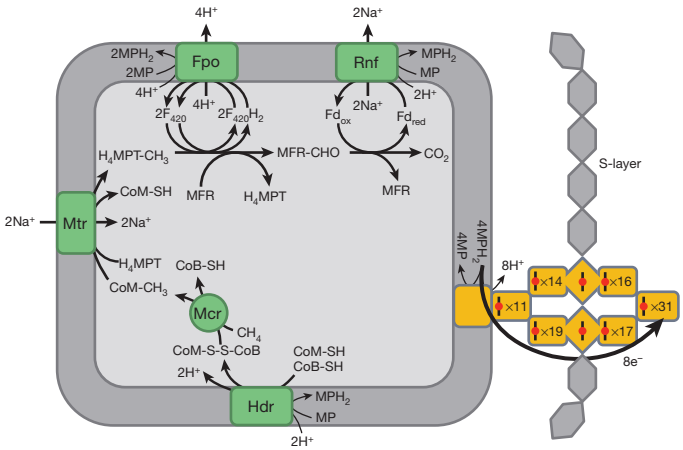

Figure 4 | A proposal for the energy metabolism of ANME-2a. The syntrophic half-reaction for ANME-2a is $CH_4 + 2H_2O \rightarrow CO_2 + 8e^- + 8H^+$. Reducing equivalents from methane are generated through the methyl branch of the Wood–Ljungdahl pathway and are deposited in the membrane-bound methanophenazine pool (Mp/MpH_2) via reactions at the Hdr, Fpo, and Rnf complexes, which oxidize CoM-SH/CoB-SH, $F_{420}H_2$, and Fd_{red}, respectively. All proteins involved in the reverse methanogenesis pathway (green) have been identified in the ANME-2a genome[27]. We have identified proteins (orange) in the ANME-2 genomes that may be responsible for extracellular electron transport as outlined in the text. Haem groups are shown schematically as in Fig. 3, and the number of haems predicted to be bound by the peptide (CxxCH motifs) is indicted.

Note added in proof: While this manuscript was in review, a paper noting the presence of large multi-haem cytochromes in archaea, including the ANME-2d genome, was published[41].

Online Content Methods, along with any additional Extended Data display items and Source Data, are available in the online version of the paper; references unique to these sections appear only in the online paper.

Received 6 March; accepted 10 August 2015.
Published online 16 September 2015.

1. Tolker-Nielsen, T. & Molin, S. Spatial organization of microbial biofilm communities. *Microb. Ecol.* **40,** 75–84 (2000).

2. Rickard, A. H., Gilbert, P., High, N. J., Kolenbrander, P. E. & Handley, P. S. Bacterial coaggregation: an integral process in the development of multi-species biofilms. *Trends Microbiol.* **11,** 94–100 (2003).
3. Battin, T. J. *et al.* Microbial landscapes: new paths to biofilm research. *Nature Rev. Microbiol.* **5,** 76–81 (2007).
4. Kim, H. J., Boedicker, J. Q., Choi, J. W. & Ismagilov, R. F. Defined spatial structure stabilizes a synthetic multispecies bacterial community. *Proc. Natl Acad. Sci. USA* **105,** 18188–18193 (2008).
5. Wintermute, E. H. & Silver, P. A. Dynamics in the mixed microbial concourse. *Genes Dev.* **24,** 2603–2614 (2010).
6. Wessel, A. K., Hmelo, L., Parsek, M. R. & Whiteley, M. Going local: technologies for exploring bacterial microenvironments. *Nature Rev. Microbiol.* **11,** 337–348 (2013).
7. Momeni, B., Brileya, K. A., Fields, M. W. & Shou, W. Strong inter-population cooperation leads to partner intermixing in microbial communities. *eLife* **2,** e00230 (2013).
8. Kempes, C. P., Okegbe, C., Mears-Clarke, Z., Follows, M. J. & Dietrich, L. E. P. Morphological optimization for access to dual oxidants in biofilms. *Proc. Natl Acad. Sci. USA* **111,** 208–213 (2014).
9. Nielsen, A. T., Tolker-Nielsen, T., Barken, K. B. & Molin, S. Role of commensal relationships on the spatial structure of a surface-attached microbial consortium. *Environ. Microbiol.* **2,** 59–68 (2000).
10. Boetius, A. *et al.* A marine microbial consortium apparently mediating anaerobic oxidation of methane. *Nature* **407,** 623–626 (2000).
11. Orphan, V. J., House, C. H., Hinrichs, K. U., McKeegan, K. D. & DeLong, E. F. Methane-consuming archaea revealed by directly coupled isotopic and phylogenetic analysis. *Science* **293,** 484–487 (2001).
12. Orcutt, B. & Meile, C. Constraints on mechanisms and rates of anaerobic oxidation of methane by microbial consortia: process-based modeling of ANME-2 archaea and sulfate reducing bacteria interactions. *Biogeosciences* **5,** 1587–1599 (2008).
13. Alperin, M. J. & Hoehler, T. M. Anaerobic methane oxidation by archaea/sulfate-reducing bacteria aggregates: 1. thermodynamic and physical constraints. *Am. J. Sci.* **309,** 869–957 (2009).
14. Orphan, V. J., House, C. H., Hinrichs, K.-U., McKeegan, K. D. & DeLong, E. F. Multiple archaeal groups mediate methane oxidation in anoxic cold seep sediments. *Proc. Natl Acad. Sci. USA* **99,** 7663–7668 (2002).
15. Knittel, K., Lösekann, T., Boetius, A., Kort, R. & Amann, R. Diversity and distribution of methanotrophic archaea at cold seeps. *Appl. Environ. Microbiol.* **71,** 467–479 (2005).
16. Orphan, V. J., Turk, K. A., Green, A. M. & House, C. H. Patterns of ^{15}N assimilation and growth of methanotrophic ANME-2 archaea and sulfate-reducing bacteria within structured syntrophic consortia revealed by FISH-SIMS. *Environ. Microbiol.* **11,** 1777–1791 (2009).
17. Nauhaus, K., Boetius, A., Krüger, M. & Widdel, F. *In vitro* demonstration of anaerobic oxidation of methane coupled to sulphate reduction in sediment from a marine gas hydrate area. *Environ. Microbiol.* **4,** 296–305 (2002).
18. Thauer, R. K. Anaerobic oxidation of methane with sulfate: on the reversibility of the reactions that are catalyzed by enzymes also involved in methanogenesis from CO_2. *Curr. Opin. Microbiol.* **14,** 292–299 (2011).
19. Moran, J. J. *et al.* Methyl sulfides as intermediates in the anaerobic oxidation of methane. *Environ. Microbiol.* **10,** 162–173 (2008).
20. Milucka, J. *et al.* Zero-valent sulphur is a key intermediate in marine methane oxidation. *Nature* **491,** 541–546 (2012).
21. Dolfing, J. The energetic consequences of hydrogen gradients in methanogenic ecosystems. *FEMS Microbiol. Ecol.* **101,** 183–187 (1992).
22. Schink, P. B. & Stams, A. J. M. in *The Prokaryotes* (eds Rosenberg, E., DeLong, E. F., Lory, S., Stackebrandt, E. & Thompson, F.) 471–493 (Springer, 2013).
23. Hoehler, T. M., Alperin, M. J., Albert, D. B. & Martens, C. S. Field and laboratory studies of methane oxidation in an anoxic marine sediment — evidence for a methanogen-sulfate reducer consortium. *Glob. Biogeochem. Cycles* **8,** 451–463 (1994).
24. Krüger, M., Wolters, H., Gehre, M., Joye, S. B. & Richnow, H.-H. Tracing the slow growth of anaerobic methane-oxidizing communities by (15)N-labelling techniques. *FEMS Microbiol. Ecol.* **63,** 401–411 (2008).
25. Schreiber, L., Holler, T., Knittel, K., Meyerdierks, A. & Amann, R. Identification of the dominant sulfate-reducing bacterial partner of anaerobic methanotrophs of the ANME-2 clade. *Environ. Microbiol.* **12,** 2327–2340 (2010).
26. Lovley, D. R. Electromicrobiology. *Annu. Rev. Microbiol.* **66,** 391–409 (2012).
27. Michelusi, N., Pirbadian, S., El-Naggar, M. Y. & Mitra, U. A stochastic model for electron transfer in bacterial cables. *IEEE J. Sel. Areas Comm.* **32,** 2402–2416 (2014).
28. Meysman, F. J. R., Risgaard-Petersen, N., Malkin, S. Y. & Nielsen, L. P. The geochemical fingerprint of microbial long-distance electron transport in the seafloor. *Geochim. Cosmochim. Acta* **152,** 122–142 (2015).
29. Meyerdierks, A. *et al.* Metagenome and mRNA expression analyses of anaerobic methanotrophic archaea of the ANME-1 group. *Environ. Microbiol.* **12,** 422–439 (2010).
30. Wang, F.-P. *et al.* Methanotrophic archaea possessing diverging methane-oxidizing and electron-transporting pathways. *ISME J.* **8,** 1069–1078 (2014).
31. Haroon, M. F. *et al.* Anaerobic oxidation of methane coupled to nitrate reduction in a novel archaeal lineage. *Nature* **500,** 567–570 (2013).
32. Strycharz-Glaven, S. M., Snider, R. M., Guiseppi-Elie, A. & Tender, L. M. On the electrical conductivity of microbial nanowires and biofilms. *Energy Environ. Sci.* **4,** 4366–4379 (2011).
33. Richardson, D. J. *et al.* The 'porin-cytochrome' model for microbe-to-mineral electron transfer. *Mol. Microbiol.* **85,** 201–212 (2012).
34. Okamoto, A., Hashimoto, K. & Nakamura, R. Long-range electron conduction of *Shewanella* biofilms mediated by outer membrane C-type cytochromes. *Bioelectrochemistry* **85,** 61–65 (2012).
35. Graham, R. C. & Karnovsky, M. J. The early stages of absorption of injected horseradish peroxidase in the proximal tubules of mouse kidney: ultrastructural cytochemistry by a new technique. *J. Histochem. Cytochem.* **14,** 291–302 (1966).
36. Litwin, J. A. Transition metal-catalysed oxidation of 3,3′-diaminobenzidine [DAB] in a model system. *Acta Histochem.* **71,** 111–117 (1982).
37. Welte, C. & Deppenmeier, U. Bioenergetics and anaerobic respiratory chains of aceticlastic methanogens. *Biochim. Biophys. Acta* **1837,** 1130–1147 (2014).
38. Summers, Z. M. *et al.* Direct exchange of electrons within aggregates of an evolved syntrophic coculture of anaerobic bacteria. *Science* **330,** 1413–1415 (2010).
39. Rotaru, A.-E. *et al.* Direct interspecies electron transfer between *Geobacter metallireducens* and *Methanosarcina barkeri*. *Appl. Environ. Microbiol.* **80,** 4599–4605 (2014).
40. Beal, E. J., House, C. H. & Orphan, V. J. Manganese- and iron-dependent marine methane oxidation. *Science* **325,** 184–187 (2009).
41. Kletzin, A. *et al.* Cytochromes *c* in Archaea: distribution, maturation, cell architecture and the special case of *Ignicoccus hospitalis*. *Front. Microbiol.* **6,** 439 (2015).

Supplementary Information is available in the online version of the paper.

Acknowledgements We are grateful for the use of the facilities of the Beckman Resource Center for Transmission Electron Microscopy at Caltech (BRCem) and advice provided by A. McDowall, our collaborators T. Deerinck and M. Ellisman from the National Center for Microscopy and Imaging Research (NCMIR), C. Miele (UGA) and M. El-Naggar at USC. Metagenomic binning of ANME-2b was conducted by C. Skennerton and M. Haroon in collaboration with G. Tyson and M. Imelfort (University of Queensland). This work was supported by the US Department of Energy, Office of Science, Office of Biological Environmental Research under award numbers (DE-SC0004949 and DE-SC0010574) and a grant from the Gordon and Betty Moore foundation Marine Microbiology Initiative (grant number 3780). V.J.O. is supported by a DOE-BER early career grant (DE-SC0003940). S.E.M. acknowledges support from an Agouron Geobiology Option post-doctoral fellowship in the Division of Geological and Planetary Sciences at Caltech and C.P.K. was supported by the NASA Astrobiology Institute (award number NNA13AA92A). This is NAI-Life Underground Publication 049.

Author Contributions V.J.O., S.M. and G.L.C. devised the study, S.M. and G.L.C. conducted the experiments and analyses and C.P.K. conducted the diffusion and electrical conductivity modelling, and all authors contributed to data interpretation and writing of the manuscript.

Author Information Sequence for the ANME-2b multi-haem cytochrome protein was deposited in GenBank under the accession number KR811028. Reprints and permissions information is available at www.nature.com/reprints. The authors declare no competing financial interests. Readers are welcome to comment on the online version of the paper. Correspondence and requests for materials should be addressed to V.J.O. (vorphan@gps.caltech.edu).

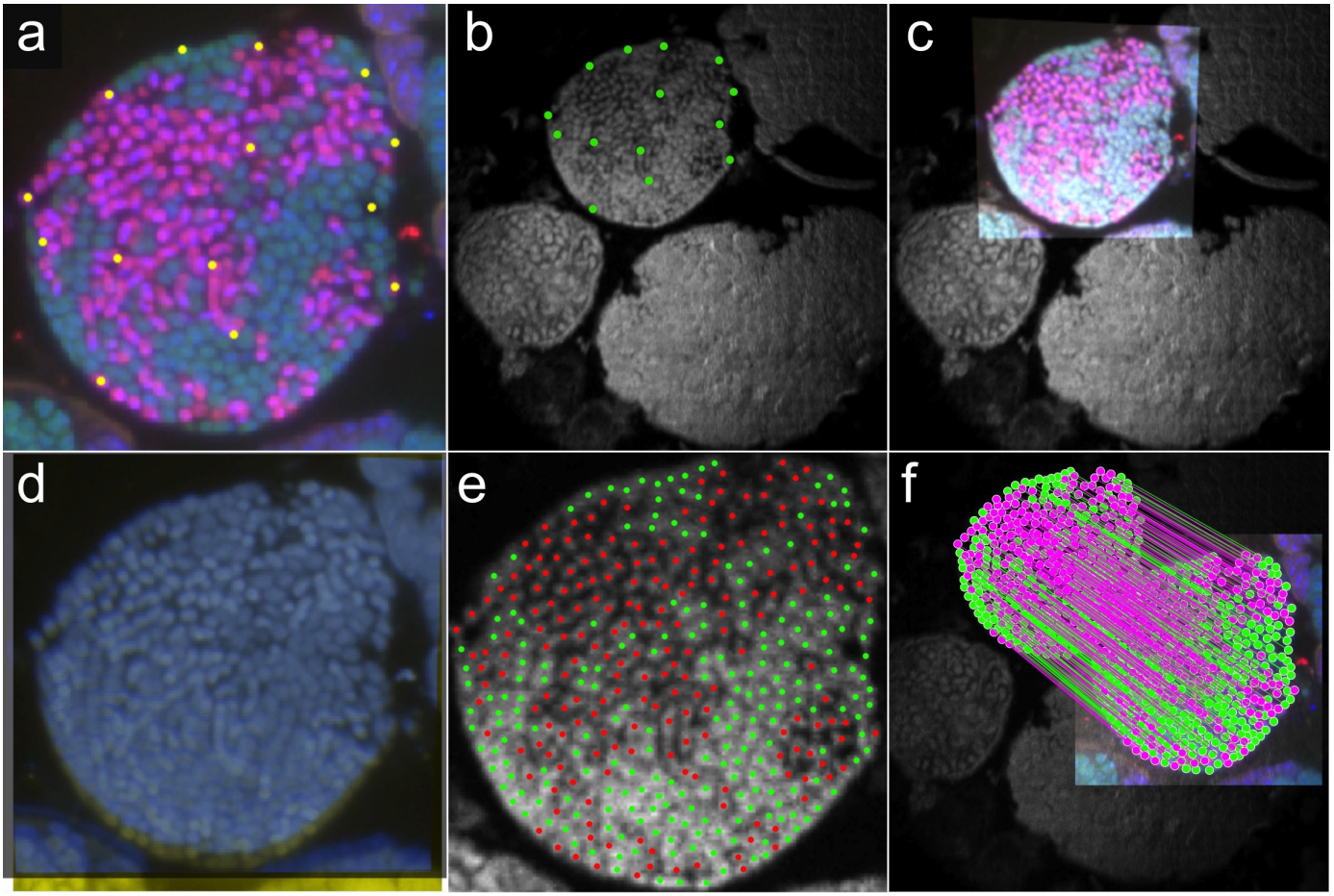

Extended Data Figure 1 | Image processing workflow for single cell correlation between FISH and nanoSIMS data sets. Representative example of data processing for an AOM consortium. **a**, Fiducial markers added to the FISH image. Marker points are shown in yellow, bacterial cells in red, archaeal cells in green. **b**, Corresponding fiducial markers identified on the nanoSIMS image. **c**, Overlay of the warped FISH image onto the nanoSIMS image, the transform function was defined by the points shown in **a** and **b**. **d**, Overlay of the original FISH image (yellow) and the warped FISH image (blue) highlighting a slight offset which becomes significant at single-cell resolutions. **e**, Centroids of the hand-drawn ROIs displayed on the nanoSIMS image, bacteria in red, archaea in green. **f**, Inverse transform applied to the ROIs drawn on the nanoSIMS image, bringing the centroid coordinates into 'FISH space' where we have more accurate measurement of distances between points.

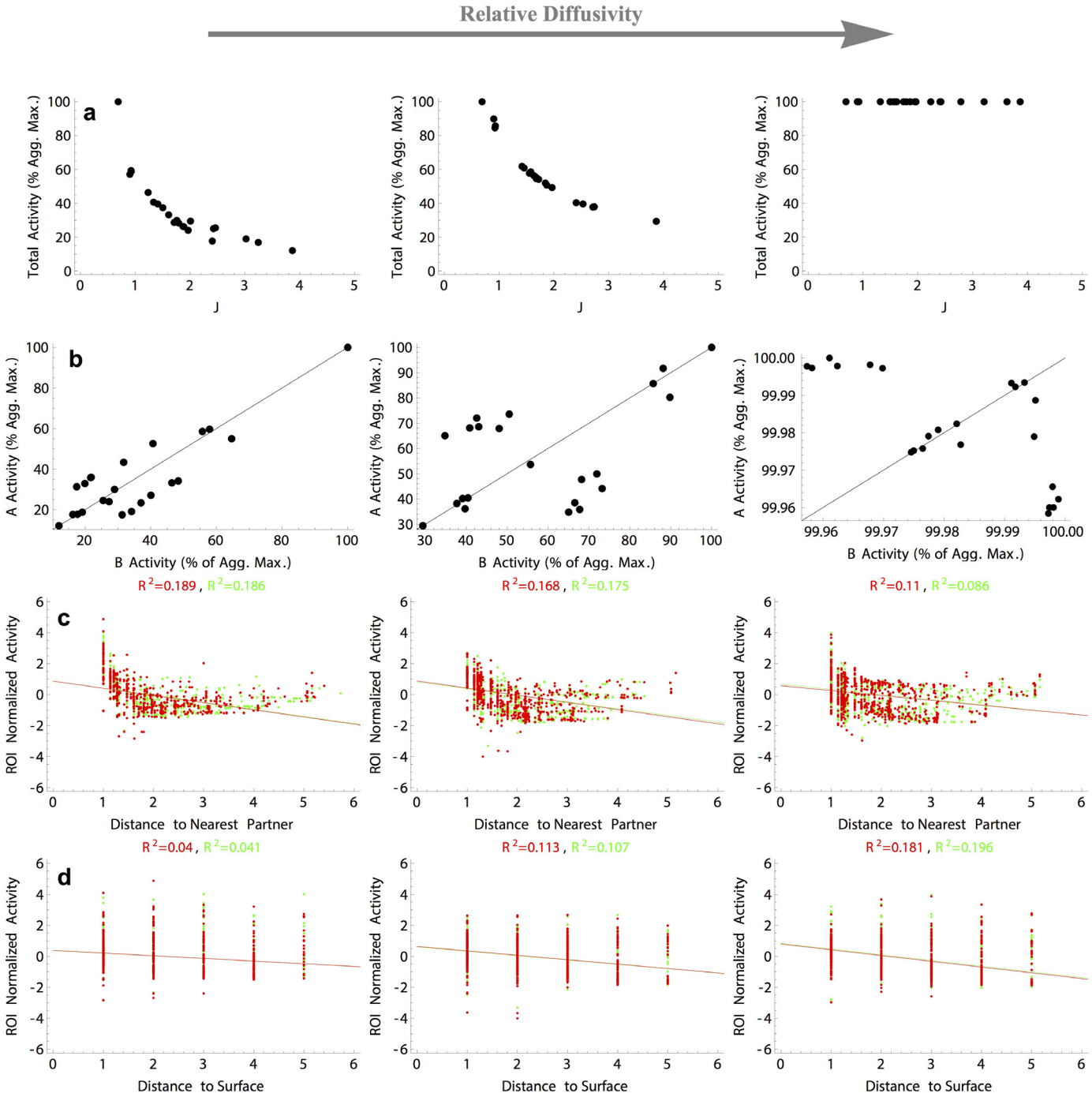

Extended Data Figure 2 | Spatial and geometric relationships for modelled aggregate geometries (well mixed to segregated) as a function of relative diffusivity (the ratio of growth rates to growth yields and diffusivity; see Supplementary Information) within the intermediate exchange model. Slow diffusion is on the left (equivalent to roughly half the relative diffusivity of hydrogen compared to measured growth rates in our system) and fast on the right (equivalent to 10^3 times faster relative diffusivity than hydrogen compared with measured growth rates; see Supplementary Information). **a**, Total aggregate activity normalized to the group maximum as a function of the J spatial metric showing a strong dependency on geometry favouring well mixed (low J value) geometries under slow relative diffusion (left) and almost no relationship with J in fast-diffusion models (right). The average activity, normalized across all of the regimes rather than within a single regime, also changes dramatically from 0.002 to 0.99 as the relative diffusivity is increased. **b**, Total normalized archaeal population activity plotted against the total bacterial population activity within the same modelled aggregate. The total number of *in silico* consortia for rows **a** and **b** is 23. **c**, The normalized (*z*-score) activity for archaea (red) and bacteria (green) plotted against the distance to the nearest three partners. **d**, The *z*-score activity for archaea (green) and bacteria (red) plotted against the distance to environment-aggregate interface (that is, aggregate surface). In plots **c** and **d** the *r*-squared values for each correlation are given at the top of each plot in colours that correspond to the two cell types. The number of modelled *in silico* bacterial and archaeal cells from **c** and **d** plotted in the columns from left to right are: 1,138 bacterial and 1,162 archaeal cells; 1,163 bacterial and 1,137 archaeal cells; and 1,153 bacterial and 1,147 archaeal cells. As diffusion is increased in these models from left to right, the organisms within consortia become less dependent on each other and instead become less syntrophically coupled, relying on environmental exchange. This leads to the highest average activity rates per consortia (compare the top panel **a** to **b**).

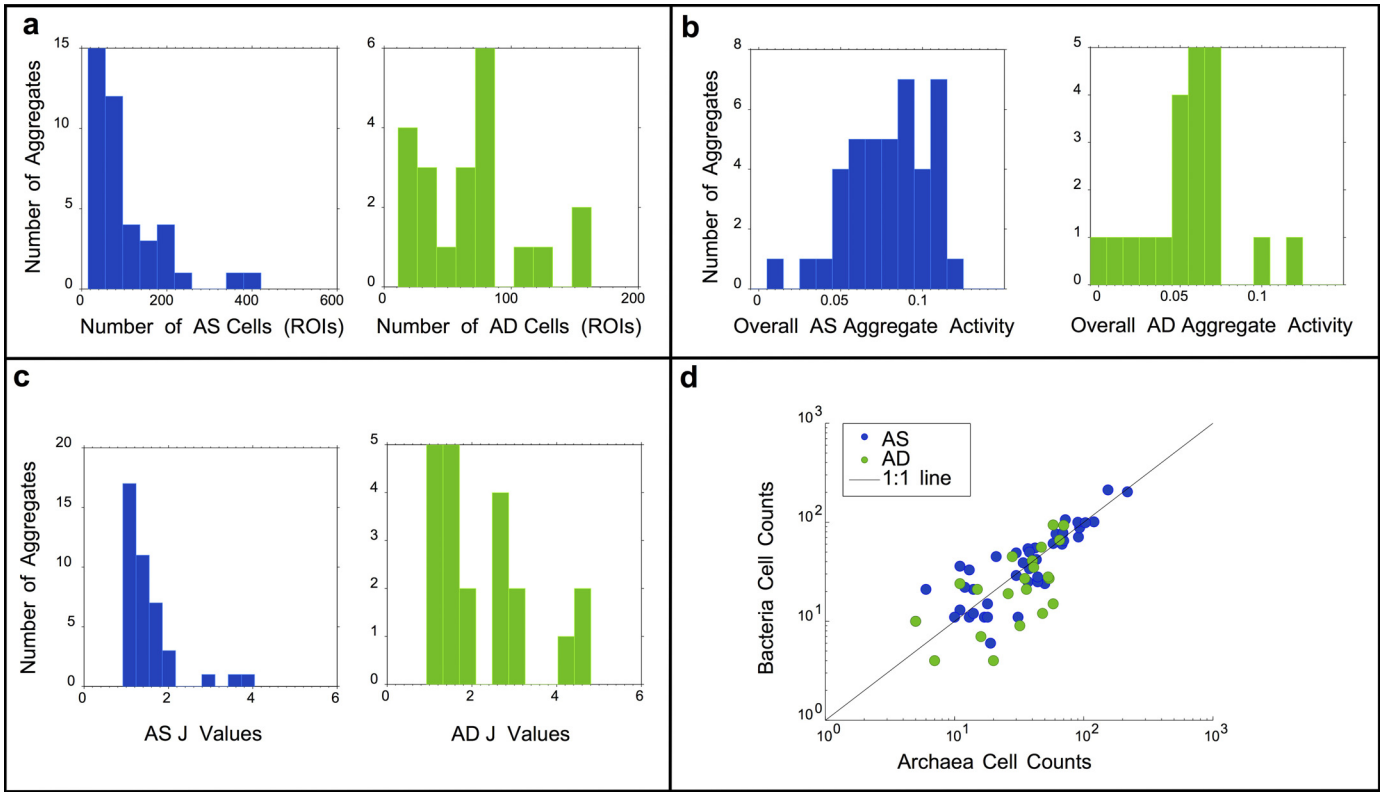

Extended Data Figure 3 | Summary of aggregate characteristics. **a**, Histograms displaying the distribution of cell counts per aggregate for AS and AD consortia, blue and green respectively. **b**, Histograms displaying the average activity values for the AS and AD consortia, where anabolic activity is measured as fractional abundance of ^{15}N per cell. **c**, Histograms of the number of AS and AD consortia associated with different levels of spatial mixing between syntrophic partners represented by the spatial mixing metric 'J' (see Supplementary Discussion for details on this metric). **d**, One-to-one relation between bacterial and archaeal cell counts in the AS and AD consortia analysed in this study. For all panels, the data set consists of 41 AS and 21 AD consortia. The number of cells in each aggregate can be found in the Source Data.

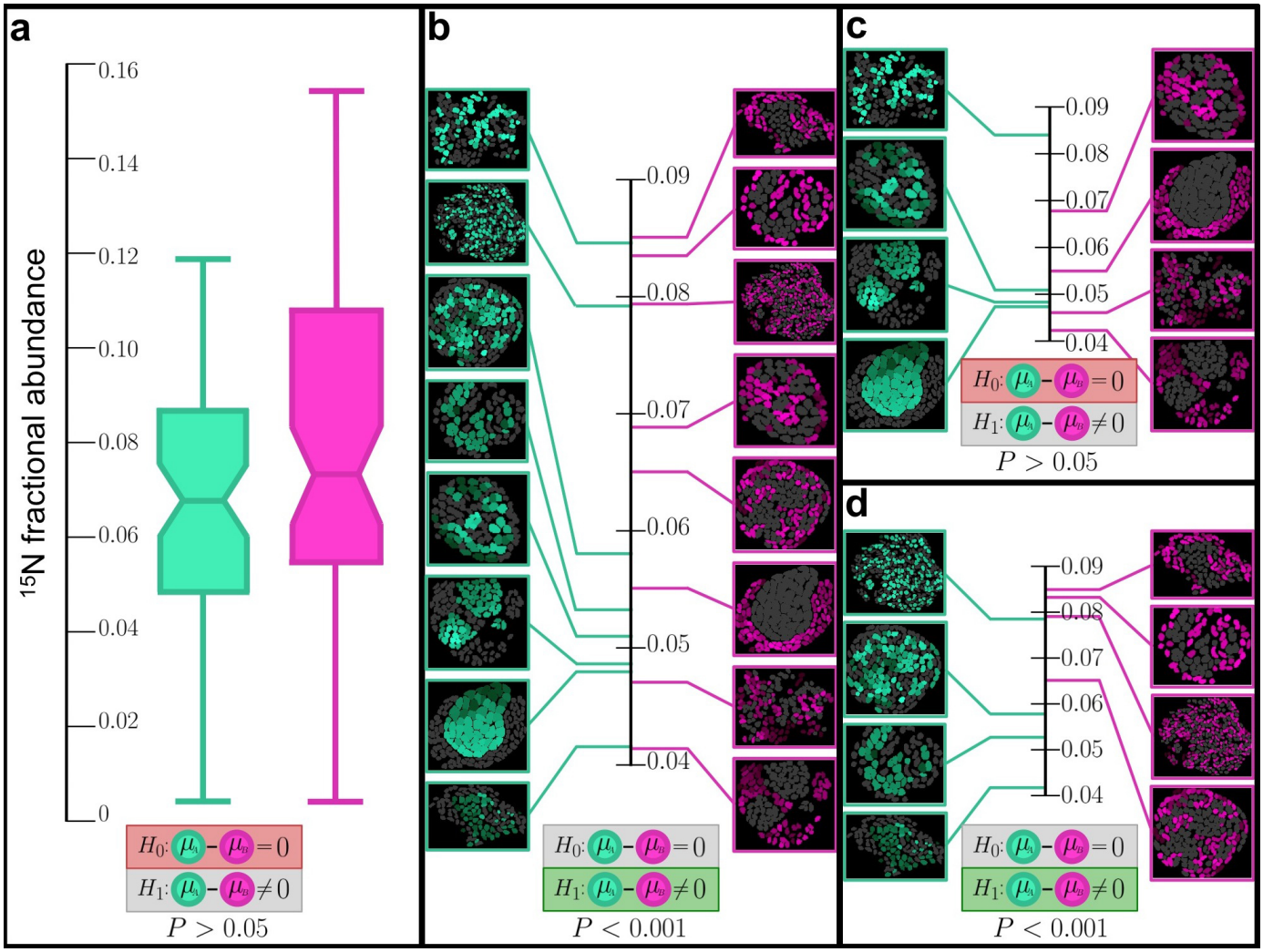

Extended Data Figure 4 | Illustration of the value of single-cell resolution activity analysis. **a**, Box plots showing the full range of archaeal and bacterial single-cell activities determined by $^{15}NH_4^+$ assimilation. The difference between the archaeal and bacterial mean activities across all aggregates ($n = 62$) is not significant (two sample *t*-test, $P > 0.05$). **b**, With our ability to quantify the activity for individual phylogenetically identified cells in AOM consortia, the average activity of the bacterial and archaeal populations within each consortium was revealed. Assessed at the level of paired populations, a significant difference in activity between the population of archaea and Deltaproteobacteria within aggregates is evident ($n = 62$, paired-sample *t*-test, $P < 0.001$). **c**, **d**, Adding phylogenetic resolution to this analysis by sub-grouping consortia based on their different deltaproteobacterial partners (AD and AS) reveals the difference between bacteria and archaea is only significant in the AS consortia ($n = 41$, paired-sample *t*-test, $P < 0.001$), while this population level offset in activity was not statistically supported within the AD group ($n = 21$, paired-sample *t*-test, $P > 0.05$), illustrating differential patterns in activity related to species membership. All axes represent ^{15}N fractional abundance. The 8 consortia images shown in panels **b**–**d** represent a subset of the total 62 consortia included in the analysis, with each image coloured by either archaeal ^{15}N enrichment on the left (green) or bacterial ^{15}N enrichment on the right (pink). The degree of brightness for each cell in the image reflects increasing levels of relative cellular ^{15}N enrichment and the average population value for ^{15}N fractional abundance is provided on the central axis.

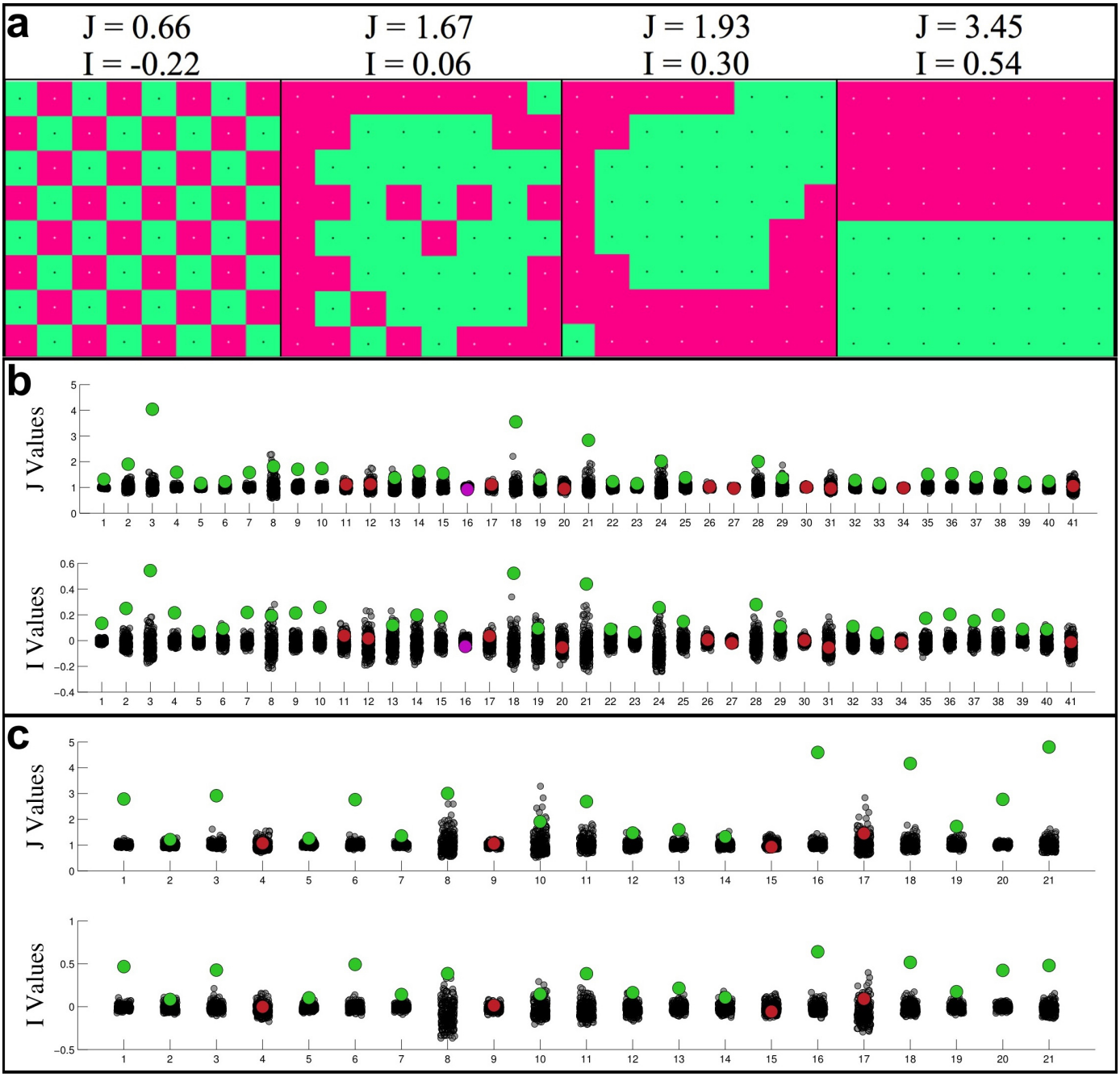

Extended Data Figure 5 | Evaluation of metrics for partner mixing. The degree of partner intermixing within an aggregate was calculated using two metrics (see Supplementary Information for detailed description of metrics). For the modified join metric (J), 1 represents random mixing, while for Moran's *I*, 0 represents random mixing. For both metrics increasing positive values represent increasing partner segregation and increasing negative values represent increasing ordered mixing (like a checkerboard). **a**, Examples of mock aggregates which were used to verify the behaviour of the two metrics. **b**, **c**, The determined values for either J or Moran's *I* are represented by the large coloured data points for each of the 41 AS aggregates or 21 AD aggregates analysed in this study, respectively. The black data points represent the values for J or Moran's *I* that were calculated in 300 permutation tests where the *x* and *y* coordinates of the archaea and bacteria cells were randomly reassigned. When the observed mixing was more segregated than 95% of the random permutation tests, the data points were coloured green and considered significant. Similarly, when the observed mixing was found to be more orderly mixed than 95% of the permutation tests the data points were coloured purple. When the observed mixing was found to be less extreme in either direction than 95% of the random test aggregates the data points were coloured red. The two metrics, while different in their formulation, gave very similar results. It is noteworthy that only a single aggregate contained cells that were more mixed than random. As expected, the permutation tests hover around the random mixing values for each metric, 1 and 0 for J and *I*, respectively.

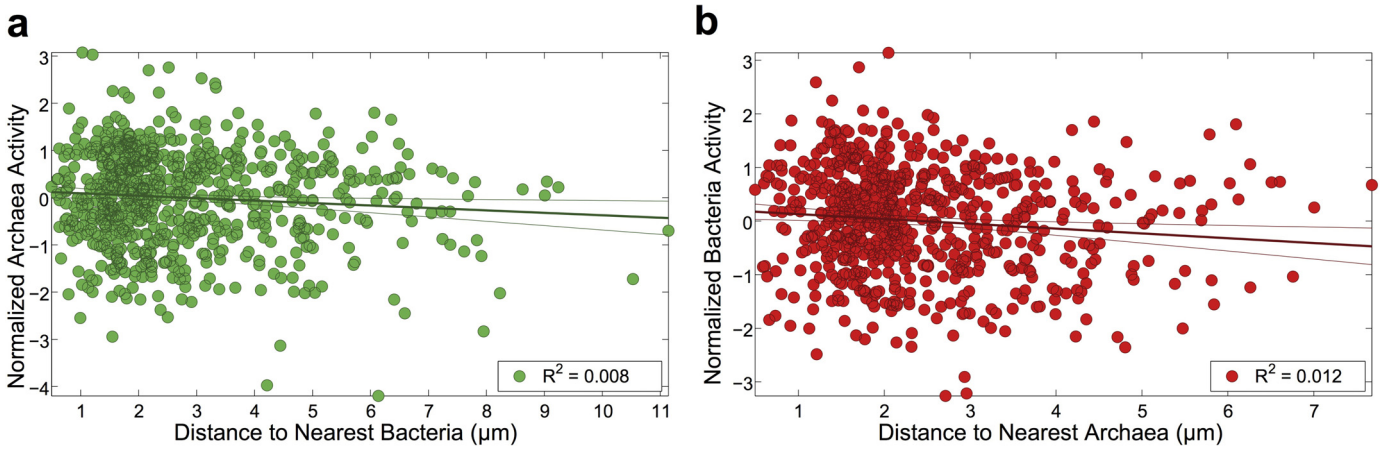

Extended Data Figure 6 | Insensitivity of cell activities to distance from nearest syntrophic partner for AD consortia. Plots displaying all ROIs analysed of a given type for consortia composed of ANME-2b or ANME-2c and Deltaproteobacteria. Normalized activity (*Z*-scores) were calculated within each aggregate to allow for comparisons between consortia with large differences in average cellular activity. **a**, Normalized activities of archaea ($n = 765$ cells) within AD consortia as a function of distance to nearest syntrophic partner. **b**, Normalized activities of bacteria ($n = 658$ cells) within AD consortia as a function of distance to nearest syntrophic partner. From this analysis, it appears that distance to nearest syntrophic partner does not account for a significant amount of the variation in cellular activity within a consortium. The R^2 values for linear regressions on the plotted data are shown in each panel. Dashed lines illustrate the 95% confidence intervals in slopes and intercepts of the linear regressions.

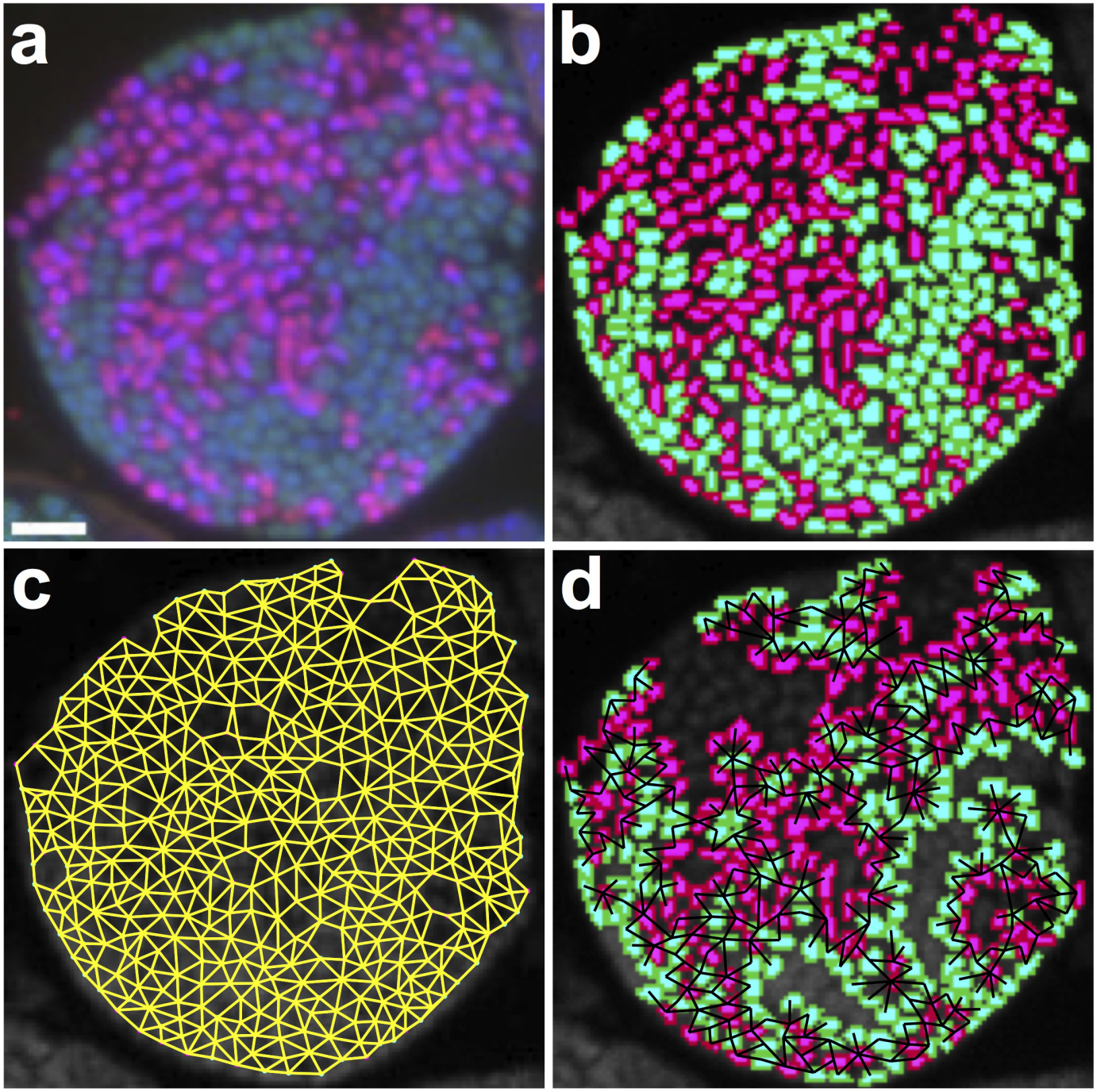

Extended Data Figure 7 | Schematic of network analysis for microbial consortia. **a**, FISH image of a representative ANME (green) and SRB (pink) consortium. **b**, Highlighted regions of interest false coloured by phylogenetic affiliation. **c**, Spheres of influence network of the consortia showing connectivity between cells. **d**, Identification of cells that share a border with a syntrophic partner (archaea adjacent to bacteria).

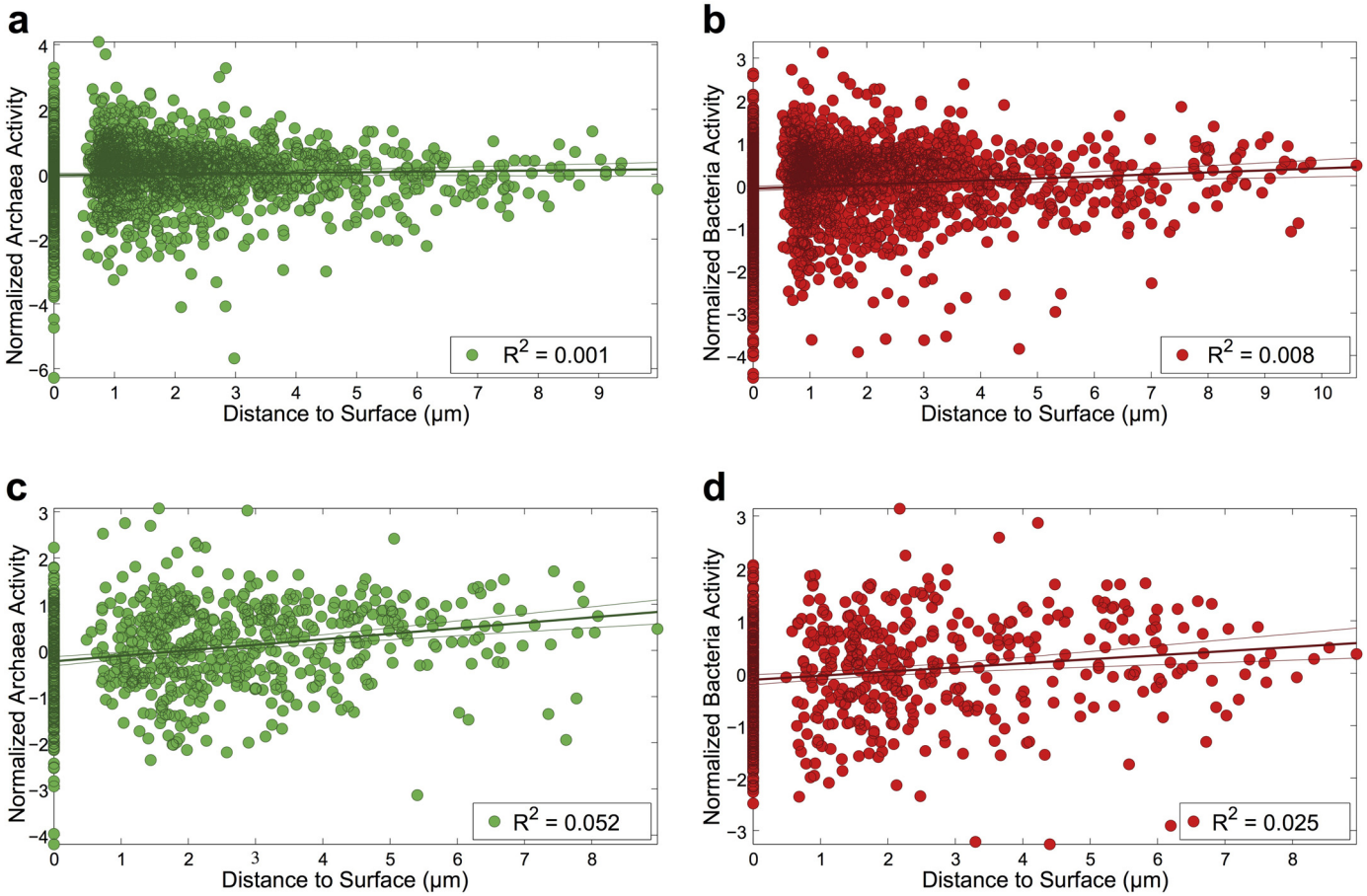

Extended Data Figure 8 | Insensitivity of cell activities to distance from surface. Plots displaying all ROIs analysed for a given population. Normalized activities (*Z*-scores) were taken within each consortium to allow for comparisons between aggregates with large differences in average cellular activity. **a**, Normalized activities of archaea within AS aggregates ($n = 1{,}967$ cells) as a function of distance to aggregate surface (that is, the external environment). **b**, Normalized activities of bacteria ($n = 2{,}063$ cells) within AS aggregates as a function of distance to aggregate surface. **c**, Normalized activities of archaea ($n = 765$ cells) within AD aggregates as a function of distance to aggregate surface. **d**, Normalized activities of bacteria ($n = 658$ cells) within AD aggregates as a function of distance to aggregate surface. From this analysis, the distance to the surface of the aggregate does not appear to explain a significant amount of the variation in cellular activity within each consortium. The R^2 values for linear regressions on the plotted data are shown in each panel. Dashed lines illustrate the 95% confidence intervals in slopes and intercepts of the linear regressions.

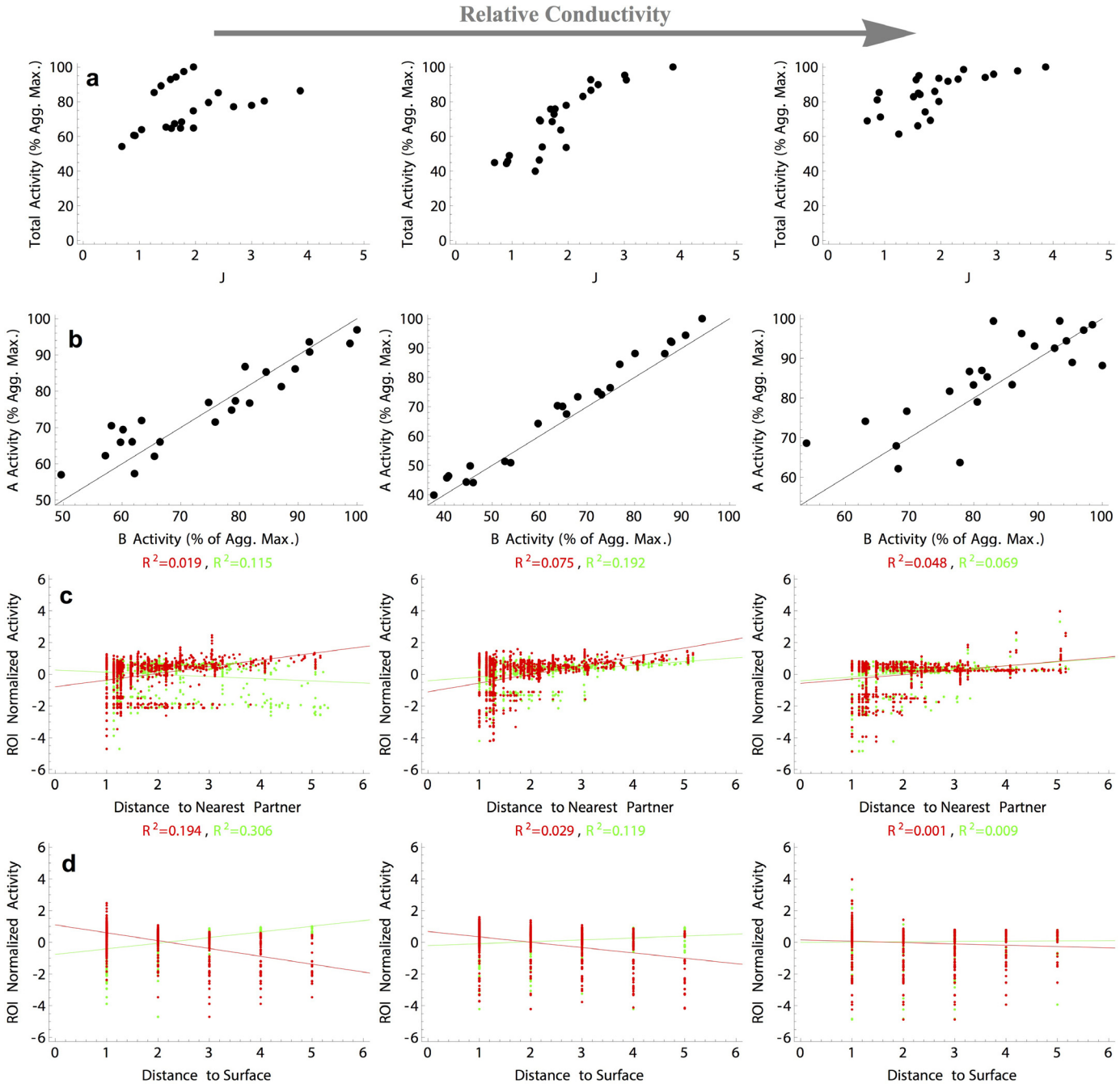

Extended Data Figure 9 | Spatial and geometric relationships for all modelled aggregate geometries as a function of relative conductivity within the direct electron transfer model. **a**, Total aggregate activity normalized to the group maximum as a function of the J spatial metric, from well-mixed (low J) to segregated (high J) aggregate geometries (23 *in silico* aggregates in total). These plots illustrate how the total activity of all of aggregate geometries changes with the relative conductivity, with less dependency on geometry observed at the fastest conductance rates. Compare to Extended Data Fig. 2: in the case of electron exchange presented here, the least mixed aggregates (high J) have the highest activity. This is because our conductive treatment of the aggregate relies on the global electric potential of each consortia, which is the strongest when the cells are spatially organized. **b**, Normalized archaeal activity plotted against the normalized bacterial activity within the same modelled aggregate. **c**, The normalized (*z*-score) activity for archaea (green) and bacteria (red) plotted against the distance to the nearest three partners. **d**, The *z*-score activity for archaea (green) and bacteria (red) plotted against the distance to environment-aggregate interface (aggregate surface). In plots **c** and **d** the *r*-squared values for each correlation are given at the top of each plot in colours that correspond to the two cell types. The number of modelled *in silico* bacterial and archaeal cells from **c** and **d** plotted in the columns from left to right are: 1,138 bacterial and 1,162 archaeal cells; 1,161 bacterial cells and 1,139 archaeal cells; and 1,134 bacterial and 1,166 archaeal cells.